Proceedings of the ASME 2007 International Design Engineering Technical Conferences & Computers and Information in Engineering Conference
IDETC/CIE 2007
September 4-7, 2007, Las Vegas, Nevada, USA

DETC2007/PTG-34078

ANALYTICAL STUDY OF HELICAL GEAR DYNAMICS WITH SLIDING FRICTION USING FLOQUET THEORY

Song He
Acoustics and Dynamics Laboratory
The Ohio State University
Columbus, OH 43210
he.81@osu.edu

Rajendra Singh*
Acoustics and Dynamics Laboratory
The Ohio State University
Columbus, OH 43210
singh.3@osu.edu

ABSTRACT
Analytical models of a helical gear pair are developed in order to examine the effect of sliding friction on the dynamic transmission error. Simplified 6 degree-of-freedom and single degree-of-freedom analytical models are developed. These models characterize the contact plane dynamics and capture the velocity reversal at the pitch line due to sliding friction. By assuming a constant mesh stiffness density along the contact lines, a linear time-varying model (with parametric excitation) is obtained. The effect of sliding friction is quantified by an effective mesh stiffness term. Floquet theory is then used to obtain closed-form solutions to the dynamic transmission error given periodic piece-wise linear tooth stiffness function. Responses to both initial conditions and forcing function under a nominal torque are derived. Analytical models are validated by comparing predictions with numerical simulations. Finally, parametrically-induced instability issues are briefly mentioned.

1 INTRODUCTION
Sliding friction is believed to be one of the major sources of gear vibration and noise especially under high toque and low speed conditions since a reversal in the sliding velocity takes place along the pitch line. Vaishya and Singh [1-3] reviewed various modeling strategies that have been historically adopted and then illustrated issues for spur gears by assuming equal load sharing among the contact teeth. This assumption leads to rectangular stiffness variations, which is a special case (with helical angle equals zero) of a more generic trapezoidal stiffness profile for helical gears. Velex and Cahouet [4] found that the dynamic bearing forces, as caused by friction at lower speeds, can generate significant time-varying excitations. Velex and Sainsot [5] examined friction excitations in errorless spur and helical gear pairs, and reported that the friction appears as a non-negligible excitation source especially for translating motions. Lundvall et al. [6] proposed a multi-body model for spur gears and briefly discussed the role of profile modification in the presence of sliding friction. Recently, we [7] have developed a more accurate model of the spur gears that includes realistic mesh stiffness and sliding friction, while overcoming the deficiency of Vaishya and Singh's work [1-3]. Further, we [8] recently proposed a 12 degrees-of-freedom (DOF), linear time-varying (LTV) analytical model for helical gears that characterizes the contact plane dynamics and captures the velocity reversal at the pitch line due to sliding friction. It includes rotational and translational motions along the line-of-action (LOA), off-line-of-action (OLOA) and axial directions. It is clear that the existing literature does not provide analytical closed form solutions for the dynamic response of a helical gear pair under the influence of sliding friction. This paper aims to fill this void.

2 PROBLEM FORMULATION
Chief objectives of this research include the following: First, analytical formulations will be proposed for a 6DOF and a simplified SDOF models to represent the helical gear system as periodically excited differential equations; we will be ignoring the auxiliary components of the gearbox and other directional properties [8]. Such simplified models allow the emphasis to be placed upon the periodical frictional effects at the tooth interface. Frictional forces and moments will be shown as parametric excitations to the piece-wisely linear effective mesh stiff of the SDOF model. Second, closed form solutions will then be derived for the LTV system in terms of dynamic transmission error (DTE) under both homogeneous and forced conditions by using the Floquet theory. Third, proposed theory will be validated by using the numerical integration method. Parametrically-induced instability under the influence of sliding friction will be briefly mentioned.

* Author of correspondence, Phone: (614) 292-9044, Fax: (614) 292-3163.

The basic scope and assumptions include: (1) The vibratory motions are small compared to the kinematical motion, so that the position of the contact lines and relative sliding velocity depend only on the mean angular motions of the gear pair. (2) The mesh stiffness per unit length along the contact line (i.e. stiffness density k) is constant [8]; this is equivalent to the equal load sharing assumption in spur gears [1-3]. (3) Coulomb's law with a constant coefficient of friction (μ) is employed [1-3, 7-8] though mixed lubrication regime exists [9]. (4) For the 6DOF model, the elastic deformations of the shaft and bearings are modeled using lumped elastic representations. For the SDOF model, however, the bearing stiffness is assumed to be much higher than the tooth mesh stiffness and thus the shaft/bearings could be simplified as rigid connections. Consequently, only the torsional DOFs are considered in terms of DTE. Also, it is assumed that the mean load is high and the dynamic load is insufficient to cause tooth separations [10].

3 6DOF LINEAR TIME-VARYING MODEL

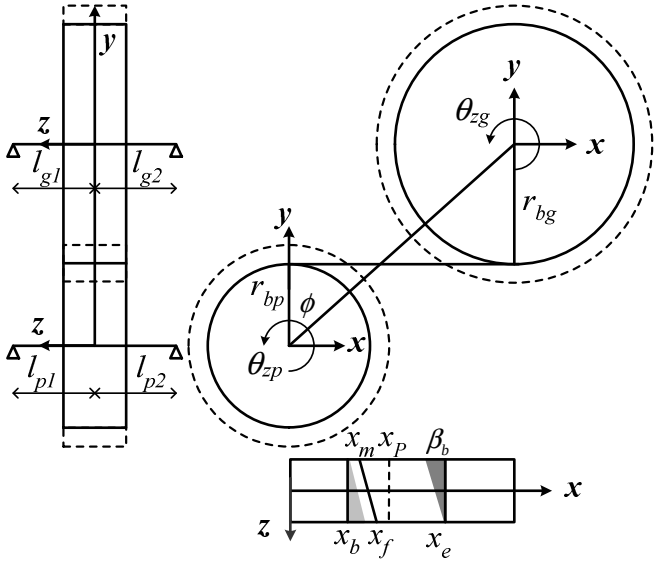

Figure 1: Schematic of the helical gear pair system.

Among the 12 DOFs [8] in the 3D helical gear pair, the axial motions as well as rotations around LOA and OLOA directions are relatively insignificant. Consequently, a simplified 6DOF model is derived including axial rotations and translational motions in the LOA and OLOA directions. The helical gear system is depicted in Fig. 1, where the pinion and gear are modeled as rigid cylinders linked by a series of independent stiffness elements that describe the contact plane tangent to the base cylinders. The normal direction at a point of contact lies in the contact plane and is perpendicular to the line of contact. The pinion and gear dynamics are formulated in the coordinate systems located at their respective centers as shown in Fig. 1. The nominal motions of the pinion and gear are given as $-\Omega_p e_z$ and $\Omega_g e_z = e_z \Omega_p r_{bp} / r_{bg}$, respectively. Here, z axis coincidences with the axial direction, e is the unit directional vector and r_{bp} and r_{bg} are the base radii of pinion and gear. An (static) input torque T_p is applied to the pinion and the (static) braking torque T_g on the gear obeys the basic gear kinematics. Superposed on the kinematic motions are rotational vibratory motions denoted by θ_{zp} and θ_{zg} for the pinion and gear. Here, analytical formulations are demonstrated via the following example case with parameters of the pinion (relevant gear parameters are within the parenthesis): number of teeth 25 (31); outside diameter 3.38 (4.13) in.; pitch diameter 3.125 (3.875) in.; root diameter 2.811 (3.561) in.; center distance 3.5 in.; transverse diametral pitch 8 in.$^{-1}$; transverse pressure angle 25°; helix angle 21.5°; face width 1.25 in.; polar moment of inertia 8.33E-3 (1.64E-2) lb-s^2-in.; mass 1.26E-2 (1.58E-2) lb-s^2/in.. Since the overall contact ratio is around 2.7, either two or three tooth pairs are in contact at any time instant. The three meshing tooth pairs within one mesh cycle are numbered as #0, #1 and #2, respectively. A constant mesh stiffness density (k) along the contact lines could be estimated by performing a static analysis using the FE/CM formulation [11].

Denote the LOA, OLOA and axial axes as x, y and z axes respectively; the dynamic motions of the pinion and gear centers consist of three translations (u) and three rotations (θ) such that $u_p = \{u_{xp} \quad u_{yp} \quad \theta_{zp}\}^T$, $u_g = \{u_{xg} \quad u_{yg} \quad \theta_{zg}\}^T$. For a contact point with local coordinates (x, r_{bp}, z) in the pinion coordinate system, its global motion at time t when considered as part of the pinion is derived as:

$$u_{pc} = \begin{Bmatrix} u_{xp} + r_{bp}\Omega_p t - r_{bp}\theta_{zp} \\ u_{yp} - x\Omega_p t + x\theta_{zp} \\ 0 \end{Bmatrix} \tag{1a}$$

Denote x_g as the x coordinate at the gear center in the pinion coordinate system, the global motion of the contact point when it is considered as part of the gear is:

$$u_{gc} = \begin{Bmatrix} u_{xg} + r_{bg}\Omega_g t + r_{bg}\theta_{zg} \\ u_{yg} - (x_g - x)\Omega_g t - (x_g - x)\theta_{zp} \\ 0 \end{Bmatrix} \tag{1b}$$

The deformation of the mesh spring is given as follows, where β_b is the helix angle:

$$\Delta_{mesh} = -\cos\beta_b \left[(u_{xp} - u_{xg}) - (r_{bp}\theta_{zp} + r_{bg}\theta_{zg}) \right] \tag{2}$$

The elemental mesh forces on the pinion and the gear are given in Eq. (3) by assuming only the elastic effects:

$$\Delta F_{mesh,p} = -\Delta F_{mesh,g} = \begin{Bmatrix} -k\Delta_{mesh}\cos\beta_b \\ \mu k \Delta_{mesh}\,\mathrm{sgn}(x - x_P) \\ k\Delta_{mesh}\sin\beta_b \end{Bmatrix} \tag{3}$$

The total mesh forces are derived by integrating the elemental forces over the contact line as given below:

$$F_{mesh,p} = -F_{mesh,g} = \begin{Bmatrix} -k\cos\beta_b \int_l \Delta_{mesh} dl \\ \mu k \int_l \Delta_{mesh}\,\mathrm{sgn}(x - x_P) dl \\ k\sin\beta_b \int_l \Delta_{mesh} dl \end{Bmatrix} \tag{4}$$

To facilitate the integration, the contact zone is divided into three regions of Fig. 1, where x_b and x_e are defined as the lower and upper boundaries of the contact zone in the LOA coordinate system of the pinion. By recognizing that $dz = dl \cdot \cos\beta_b$ and $dx = dl \cdot \sin\beta_b$, the integral in Eq. (4) yields:

$$\bar{\Delta} = \int_l \Delta_{mesh} dl = -(z_f - z_m)\left[(u_{xp} - u_{xg}) - (r_{bp}\theta_{zp} + r_{bg}\theta_{zg})\right] \quad (5)$$

The contact force $F_{mesh,p,x}$ in the LOA direction is evaluated as:

$$F_{mesh,p,x} = -k\cos\beta_b\bar{\Delta} \quad (6)$$

Due to the sliding friction, the friction force $F_{mesh,p,y}$ involves a discontinuous sign function and it needs to be evaluated separately for three different cases assuming a constant μ.

Case 1: Both limits of the contact line are less than x_P, which implies the contact line on the pinion is completely below the pitch cylinder (approach action) so that sgn($x - x_P$)= –1. The friction force of the pinion is:

$$F_{mesh,p,y} = -\mu k\bar{\Delta} \quad (7a)$$

Case 2: In the case the line of contact lies on either side of the pitch cylinder. The friction force integral must be evaluated in two parts.

$$F_{mesh,p,y} = \mu k(\bar{\Delta}_2 - \bar{\Delta}_1) \quad (7b)$$

where $\bar{\Delta}_1 = -(z_P - z_m)\left[(u_{xp} - u_{xg}) - (r_{bp}\theta_{zp} + r_{bg}\theta_{zg})\right]$,

$\bar{\Delta}_2 = -(z_f - z_P)\left[(u_{xp} - u_{xg}) - (r_{bp}\theta_{zp} + r_{bg}\theta_{zg})\right]$.

Case 3: Both limits are greater than x_P, which implies the contact line on the pinion is completely above the pitch cylinder (recess action). Consequently, sgn($x - x_P$)= 1 and the friction force on the pinion is:

$$F_{mesh,p,y} = \mu k\bar{\Delta} \quad (7c)$$

The elemental moments on the pinion at a point on the contact line are derived as:

$$\Delta M_{mesh,p} = k\Delta_{mesh}\begin{Bmatrix} r_{bp}\sin\beta_b - z\mu\,\mathrm{sgn}(x - x_P) \\ -x\sin\beta_b - z\cos\beta_b \\ x\mu\,\mathrm{sgn}(x - x_P) + r_{bp}\cos\beta_b \end{Bmatrix} \quad (8)$$

In order to obtain the total moments, two integration operations are defined over the line of contact with lower and higher limits denoted as x_l and x_h, respectively:

$$(\Delta \cdot x)(x_l, x_h) = \int_{x_l}^{x_h} x\Delta_{mesh} dl = -(x_h + x_l)(z_h - z_l)\frac{c_1}{2} \quad (9a)$$

$$(\Delta \cdot z)(x_l, x_h) = \int_{x_l}^{x_h} z\Delta_{mesh} dl = c_1\frac{(z_h^2 - z_l^2)}{2} \quad (9b)$$

where $c_1 = (u_{xp} - u_{xg}) - (r_{bp}\theta_{zp} + r_{bg}\theta_{zg})$, and axial coordinates z_h and z_l could be computed based on gear geometry. The moments of the mesh force acting on the pinion and gear are thus derived as:

$$M_{mesh,p,\theta_z} = k\begin{bmatrix} -\mu(\Delta \cdot x)(x_m, x_P) + \\ \mu(\Delta \cdot x)(x_P, x_f) + r_{bp}\bar{\Delta}\cos\beta_b \end{bmatrix} \quad (10a)$$

$$M_{mesh,g,\theta_z} = k\begin{bmatrix} x_g(\bar{\Delta}_2 - \bar{\Delta}_1) + \mu(\Delta \cdot x)(x_m, x_P) \\ -\mu(\Delta \cdot x)(x_P, x_f) + r_{bg}\bar{\Delta}\cos\beta_b \end{bmatrix} \quad (10b)$$

Note that Eqs. (6-10) are formulated for a single tooth pair in contact. For multiple tooth pairs in contact with contact ratio σ, n = ceil(σ) number of meshing tooth pairs need to be formulated, where the "ceil" function rounds σ to the nearest integers towards infinity. For the example case, three tooth pairs are considered in a single mesh cycle. Fig. 2(a) shows the contact plane and Fig. 2(b) illustrates a zoomed-in snapshot at the beginning of a mesh cycle.

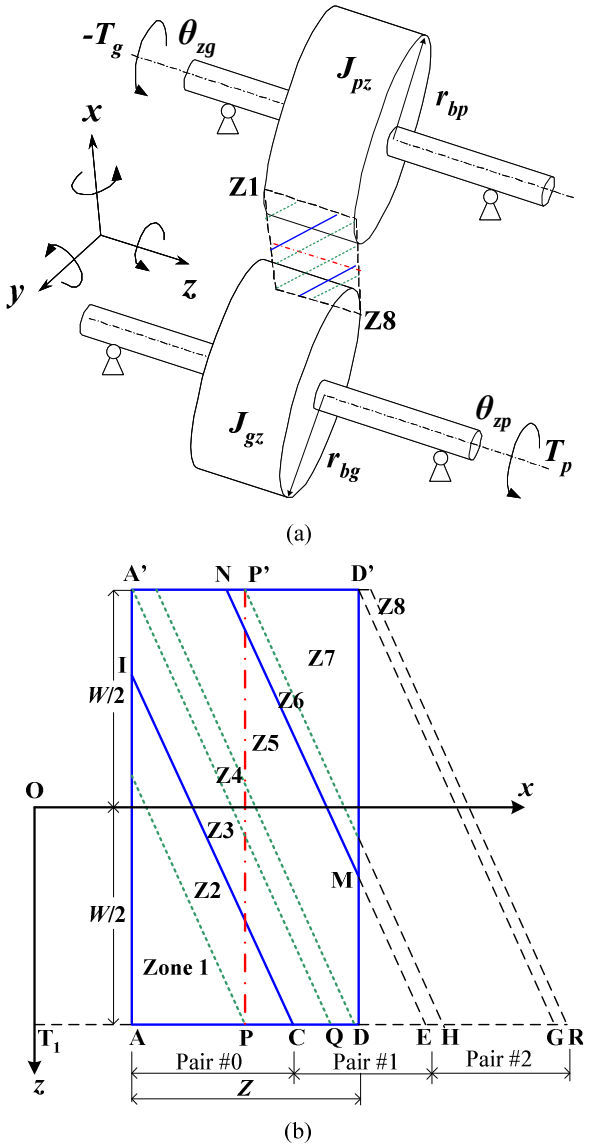

Figure 2: Contact zones at the beginning of a mesh cycle. (a) In the helical gear pair; (b) contact zones within contact plane. Key: PP' is the pitch line; AA' is the face width W; AD is the length of contact zone Z.

At the instant of Fig. 2, pair #0 just comes into mesh at point A and pair #1 is in contact along line CI. Likewise, pair #2 contacts each other along line MN. As the gears roll, the contact lines move diagonally across the contact zone. When pair #0 reaches the pitch point P, the relative sliding velocity of the pinion with respect to the gear starts to reverse, resulting in a reversal of friction force along the portion of contact line surpass the pitch point. Once pair #0 reaches the CI line (and pair #1 reaches MN line) at the end of the mesh circle, pair #0 becomes #1 (and pair #1 becomes #2) corresponding to the start of the next mesh cycle. At any time instant t, the x coordinates of the three pairs are projected along the AR line and defined as $x_0(t)$, $x_1(t)$ and $x_2(t)$ in Eq. (11). Here, λ is the base pitch, L represents the geometrical distance, and "mod" is the modulus function defined as: $\mathrm{mod}(x, y)=x-y\cdot\mathrm{floor}(x/y)$, if $y \neq 0$.

$$x_0(t) = \mathrm{mod}(\Omega_p r_{bp} t, \lambda) + L_{\mathrm{T_i A}} \tag{11a}$$

$$x_1(t) = \mathrm{mod}(\Omega_p r_{bp} t, \lambda) + \lambda + L_{\mathrm{T_i A}} \tag{11b}$$

$$x_2(t) = \mathrm{mod}(\Omega_p r_{bp} t, \lambda) + 2\lambda + L_{\mathrm{T_i A}} \tag{11c}$$

To implement the integration algorithm, the contact regions are further divided into eight contact zones as shown in Fig. 2(b). Zones 1 and 2 correspond to pair #0 before and after reaching the pitch line; Zones 3-5 and Zones 6-8 correspond to pairs #1 and #2, respectively. The zone classifications and their corresponding integration limits for the calculation of dynamic forces and moments are derived as following, where x_m, x_f, z_m and z_f denote the lower and upper limits along x and z axes.

Zone 1 ($L_{\mathrm{T_i A}} \le x_0(t) < L_{\mathrm{T_i P}}$): $x_m = L_{\mathrm{T_i A}}$, $x_f = x_0$,
$z_f = 0.5W$, $z_m = 0.5W - \left[(x_0 - L_{\mathrm{T_i A}})/\tan\beta_b\right]$ (12a)

Zone 2 ($L_{\mathrm{T_i P}} \le x_0(t) < L_{\mathrm{T_i C}}$): $x_m = L_{\mathrm{T_i A}}$, $x_f = x_0$, $x_p = L_{\mathrm{T_i P}}$,
$z_f = 0.5W$, $z_m = 0.5W - \left[(x_0 - L_{\mathrm{T_i A}})/\tan\beta_b\right]$,
$z_p = 0.5W - \left[(x_0 - L_{\mathrm{T_i P}})/\tan\beta_b\right]$ (12b)

Zone 3 ($L_{\mathrm{T_i C}} \le x_1(t) < L_{\mathrm{T_i Q}}$): $x_m = L_{\mathrm{T_i A}}$, $x_f = x_1$,
$x_p = L_{\mathrm{T_i P}}$, $z_m = 0.5W - \left[(x_1 - L_{\mathrm{T_i A}})/\tan\beta_b\right]$,
$z_f = 0.5W$, $z_p = 0.5W - \left[(x_1 - L_{\mathrm{T_i P}})/\tan\beta_b\right]$ (12c)

Zone 4 ($L_{\mathrm{T_i Q}} \le x_1(t) < L_{\mathrm{T_i D}}$): $x_m = x_1 - W\cdot\tan\beta_b$,
$x_f = x_1$, $x_p = L_{\mathrm{T_i P}}$, $z_m = -0.5W$, $z_f = 0.5W$,
$z_p = 0.5W - \left[(x_1 - L_{\mathrm{T_i P}})/\tan\beta_b\right]$ (12d)

Zone 5 ($L_{\mathrm{T_i D}} \le x_1(t) < L_{\mathrm{T_i E}}$): $x_m = x_1 - W\tan\beta_b$, $x_f = L_{\mathrm{T_i D}}$,
$x_p = L_{\mathrm{T_i P}}$, $z_f = 0.5W - \left[(x_1 - L_{\mathrm{T_i D}})/\tan\beta_b\right]$,
$z_m = -0.5W$, $z_p = 0.5W - \left[(x_1 - L_{\mathrm{T_i P}})/\tan\beta_b\right]$ (12e)

Zone 6 ($L_{\mathrm{T_i E}} \le x_2(t) < L_{\mathrm{T_i H}}$): $x_m = x_2 - W\cdot\tan\beta_b$, $x_f = L_{\mathrm{T_i D}}$,
$x_p = L_{\mathrm{T_i P}}$, $z_f = 0.5W - \left[(x_2 - L_{\mathrm{T_i D}})/\tan\beta_b\right]$,
$z_m = -0.5W$, $z_p = 0.5W - \left[(x_1 - L_{\mathrm{T_i P}})/\tan\beta_b\right]$ (12f)

Zone 7 ($L_{\mathrm{T_i H}} \le x_2(t) < L_{\mathrm{T_i G}}$): $x_m = x_2 - W\tan\beta_b$, $x_f = L_{\mathrm{T_i D}}$,
$z_m = -0.5W$, $z_f = 0.5W - \left[(x_2 - L_{\mathrm{T_i D}})/\tan\beta_b\right]$ (12g)

Zone 8 ($L_{\mathrm{T_i G}} \le x_2(t) < L_{\mathrm{T_i R}}$): No definition (12h)

Formulate the combined dynamic forces and moments of multiple contacting tooth pairs. The bearing forces acting on the pinion x and y directions are as follows, where $k_{pix(y)}$ are the bearing stiffness. The gear equations can be derived similarly.

$$F_{B,p,x} = -(k_{p1x} + k_{p2x})u_{xp} \qquad F_{B,p,y} = -(k_{p1y} + k_{p2y})u_{yp} \tag{13a,b}$$

The viscous damping forces in the x and y directions due to the bearing stiffness are derived as following by assuming viscous damping coefficients $\zeta_{p(g)ix(y)}$:

$$F_{V,p,x} = -2\left(\zeta_{p1x}\sqrt{k_{p1x}m_p} + \zeta_{p2x}\sqrt{k_{p2x}m_p}\right)\dot{u}_{xp}$$
$$F_{V,p,y} = -2\left(\zeta_{p1y}\sqrt{k_{p1y}m_p} + \zeta_{p2y}\sqrt{k_{p2y}m_p}\right)\dot{u}_{yp} \tag{14a,b}$$

The viscous damping moments around the axial direction:

$$M_{V,p,\theta_z} = -2\zeta_{Jpz}\sqrt{k_{Jpy}(t)J_{pz}/r_{bp}}\,(r_{rp}\dot{\theta}_{zp} + r_{bg}\dot{\theta}_{zg}) \tag{15}$$

The governing equations of the 6DOF model are derived as:

$$m_p\ddot{u}_{xp} = \sum_{i=0}^{n=\mathrm{floor}(\sigma)} F_{mesh,p,x,i} + \sum_{j=1}^{2} F_{B,p,x,j} + \sum_{j=1}^{2} F_{V,p,x,j} \tag{16a}$$

$$m_p\ddot{u}_{yp} = \sum_{i=0}^{n=\mathrm{floor}(\sigma)} F_{mesh,p,y,i} + \sum_{j=1}^{2} F_{B,p,y,j} + \sum_{j=1}^{2} F_{V,p,y,j} \tag{16b}$$

$$J_{zp}\ddot{\theta}_{zp} = \sum_{i=0}^{n=\mathrm{floor}(\sigma)} M_{mesh,p,\theta_z,i} + M_{V,p,\theta_z} + T_p \tag{16c}$$

$$m_g\ddot{u}_{xg} = \sum_{i=0}^{n=\mathrm{floor}(\sigma)} F_{mesh,g,x,i} + \sum_{j=1}^{2} F_{B,g,x,j} + \sum_{j=1}^{2} F_{V,g,x,j} \tag{17a}$$

$$m_g\ddot{u}_{yg} = \sum_{i=0}^{n=\mathrm{floor}(\sigma)} F_{mesh,g,y,i} + \sum_{j=1}^{2} F_{B,g,y,j} + \sum_{j=1}^{2} F_{V,g,y,j} \tag{17b}$$

$$J_{zg}\ddot{\theta}_{zg} = \sum_{i=0}^{n=\mathrm{floor}(\sigma)} M_{mesh,g,\theta_z,i} + M_{V,g,\theta_z} - T_g \tag{17c}$$

The role of sliding friction is illustrated in Fig. 3 by comparing time domain responses of u_{xp}, u_{yp} and DTE at T_p = 2000 lb-in and Ω_p =1000 RPM for μ = 0.01 and μ = 0.1. Observe that sliding friction has most significant effect in the OLOA dynamics and has a moderate influence in the LOA direction. Although the DTE tends to be less sensitive to variations in the sliding friction, note that the amplitude of DTE is higher than those of u_{xp} and u_{yp} by at least two orders of magnitude. Further, a careful comparative study shows that the second harmonic of DTE is most significantly amplified due to friction. These observations are consistent with predictions of the 12DOF model [8] with reduced modeling and computational costs. Hence, the proposed 6DOF model is easier to be implemented for parametric design studies.

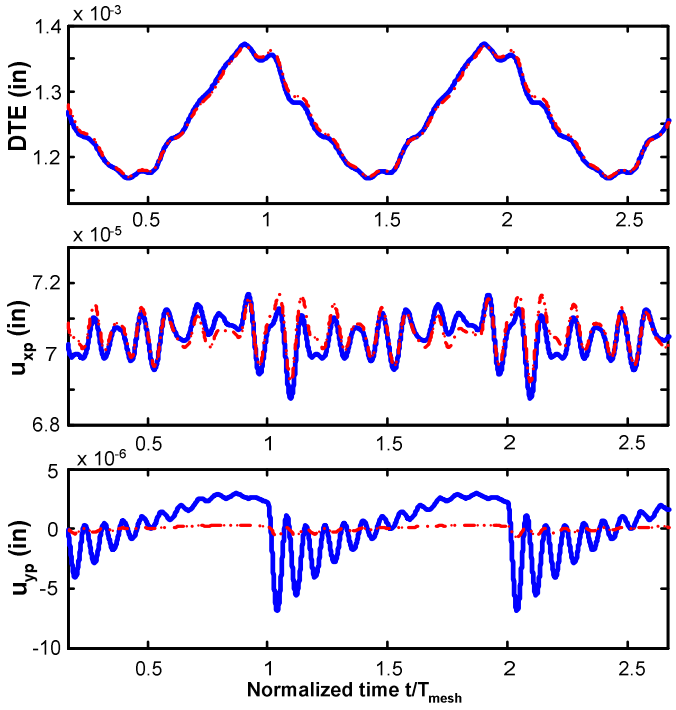

Figure 3: Time domain responses of pinion displacements u_{xp}, u_{yp} and DTE at T_p = 2000 lb-in and Ω_p = 1000 RPM. Key: ——, μ = 0.1; – · – μ = 0.01.

4 SDOF LINEAR TIME-VARYING SYSTEM MODEL

When only the torsional DOF is of interest, a simplified SDOF model could be derived by assuming that the stiffness of the bearings are much higher than the tooth stiffness. Define DTE as $\delta(t) = r_{bp}\theta_{zp}(t) + r_{bp}\theta_{zp}(t)$; the unloaded static transmission error $\varepsilon(t)$ causes a displacement excitation at the gear mesh. Note that mesh forces oriented in other directions are still required for calculations of dynamic moments in the torsional direction. Hence, the effective torsional tooth stiffness should have contributions from both the sliding friction and the time-varying elastic tooth stiffness due to Hertzian contact.

For multiple tooth pairs in contact, the dynamic moments on the pinion $M_{p,i}(t)$ and gear $M_{g,i}(t)$ are explicitly derived for each meshing tooth pair. Define effective dynamic tooth stiffness function by considering the vibratory motions in the torsional direction including frictional effects as:

$$K_{p,i}(t) = \frac{M_{p,i}(t)}{r_{bp}\delta(t)}, \quad K_{g,i}(t) = \frac{M_{g,i}(t)}{r_{bg}\delta(t)} \quad (i = 0,1,2) \quad (18a,b)$$

Here, the first meshing tooth pair (#0), defined by Eq. (11a) and shown in Fig. 2(b), is classified into two contact zones (Z*i*) of Eqs. (12a,b). Its composite torsional stiffness are:

$$K_{p,0}(t) = \begin{cases} \dfrac{k}{2r_{bp}}\left[2r_{bp}\cos\beta_b - \mu\left(x_f(t)+x_m\right)\right]\left(z_f - z_m(t)\right), & \text{Z1} \\ \dfrac{k}{2r_{bp}}\begin{bmatrix} -\mu\left(x_p+x_m\right)\left(z_p(t)-z_m(t)\right) \\ +\mu\left(x_f(t)+x_p\right)\left(z_f - z_p(t)\right) \\ +2r_{bp}\cos\beta_b\left(z_f - z_m(t)\right) \end{bmatrix}, & \text{Z2} \end{cases} \quad (19a)$$

$$K_{g,0}(t) = \begin{cases} \dfrac{k}{2r_{bg}}\left[\mu\left(x_f(t)+x_m-2x_g\right)+2r_{bg}\cos\beta_b\right]\left(z_f - z_m(t)\right), & \text{Z1} \\ \dfrac{k}{2r_{bg}}\begin{bmatrix} \mu\left(x_p+x_m\right)\left(z_p - z_m(t)\right) - \mu\left(x_f(t)+x_p\right)\left(z_f - z_p(t)\right) \\ +2x_g\mu\left(z_f + z_m(t) - 2z_p(t)\right) + 2r_{bg}\cos\beta_b\left(z_f - z_m(t)\right) \end{bmatrix}, & \text{Z2} \end{cases} \quad (19b)$$

The second meshing tooth pair (#1), defined by Eq. (11b), is classified into three contact zones 3-5 as shown in Fig. 2(b). Its composite stiffness are derived for the pinion and gear as:

$$K_{p,1}(t) = \begin{cases} \dfrac{k}{2r_{bp}}\begin{bmatrix} -\mu\left(x_p+x_m\right)\left(z_p(t)-z_m(t)\right) + \\ \mu\left(x_f(t)+x_p\right)\left(z_f - z_p(t)\right) + 2r_{bp}\cos\beta_b\left(z_f - z_m(t)\right) \end{bmatrix}, & \text{Z3} \\ \dfrac{k}{2r_{bp}}\begin{bmatrix} -\mu\left(x_p+x_m(t)\right)\left(z_p(t)-z_m\right) + \\ \mu\left(x_f(t)+x_p\right)\left(z_f - z_p(t)\right) + 2r_{bp}\cos\beta_b\left(z_f - z_m(t)\right) \end{bmatrix}, & \text{Z4} \\ \dfrac{k}{2r_{bp}}\begin{bmatrix} -\mu\left(x_p+x_m(t)\right)\left(z_p(t)-z_m\right) + \\ \mu\left(x_f+x_p\right)\left(z_f(t)-z_p(t)\right) + 2r_{bp}\cos\beta_b\left(z_f(t)-z_m\right) \end{bmatrix}, & \text{Z5} \end{cases}$$

$$K_{g,1}(t) = \begin{cases} \dfrac{k}{2r_{bg}}\begin{bmatrix} \mu\left(x_p+x_m\right)\left(z_p(t)-z_m(t)\right) + 2x_g\mu\left(z_f + z_m(t) - 2z_p(t)\right) \\ -\mu\left(x_f(t)+x_p\right)\left(z_f - z_p(t)\right) + 2r_{bg}\cos\beta_b\left(z_f - z_m(t)\right) \end{bmatrix}, & \text{Z3} \\ \dfrac{k}{2r_{bg}}\begin{bmatrix} \mu\left(x_p+x_m(t)\right)\left(z_p(t)-z_m\right) - \mu\left(x_f(t)+x_p\right)\left(z_f - z_p(t)\right) \\ +2x_g\mu\left(z_f + z_m - 2z_p(t)\right) + 2r_{bg}\cos\beta_b\left(z_f - z_m\right) \end{bmatrix}, & \text{Z4} \\ \dfrac{k}{2r_{bg}}\begin{bmatrix} \mu\left(x_p+x_m(t)\right)\left(z_p(t)-z_m\right) - \mu\left(x_f+x_p\right)\left(z_f(t)-z_p(t)\right) \\ +2x_g\mu\left(z_f(t) + z_m - 2z_p(t)\right) + 2r_{bg}\cos\beta_b\left(z_f(t)-z_m\right) \end{bmatrix}, & \text{Z5} \end{cases} \quad (20a,b)$$

The third meshing tooth pair (#2), defined by Eq. (11c), is divided into three contact zones 6-8 as shown in Fig 2(b). Its composite stiffness are derived for the pinion and gear as:

$$K_{p,2}(t) = \begin{cases} \dfrac{k}{2r_{bp}}\begin{bmatrix} \mu\left(x_f+x_p\right)\left(z_f(t)-z_p(t)\right) + 2r_{bp}\cos\beta_b\left(z_f(t)-z_m\right) \\ -\mu\left(x_p+x_m(t)\right)\left(z_p(t)-z_m\right) \end{bmatrix}, & \text{Z6} \\ \dfrac{k}{2r_{bp}}\left[\mu\left(x_f+x_m(t)\right)+r_{bp}\cos\beta_b\right]\left(z_f(t)-z_m\right), & \text{Z7} \\ 0, & \text{Z8} \end{cases}$$

$$K_{g,2}(t) = \begin{cases} \dfrac{k}{2r_{bg}}\begin{bmatrix} \mu\left(x_p+x_m(t)\right)\left(z_p(t)-z_m\right) - \mu\left(x_f+x_p\right)\left(z_f(t)-z_p(t)\right) \\ +2x_g\mu\left(z_f(t) + z_m - 2z_p(t)\right) + r_{bg}\cos\beta_b\left(z_f(t)-z_m\right) \end{bmatrix}, & \text{Z6} \\ \dfrac{k}{2r_{bg}}\left[\mu\left(x_f+x_m(t)\right)+r_{bp}\cos\beta_b\right]\left(z_f(t)-z_m\right), & \text{Z7} \\ 0, & \text{Z8} \end{cases} \quad (21a, b)$$

The undamped equations of torsional motion for the pinion and gear are derived as follows:

$$J_{pz}\ddot{\theta}_{zp}(t)+\sum_{i=0}^{2}K_{p,i}(t)\cdot r_{bp}\cdot\left[\delta(t)-\varepsilon(t)\right]=T_p \qquad (22)$$

$$J_{gz}\ddot{\theta}_{pz}(t)+\sum_{i=0}^{2}K_{g,i}(t)\cdot r_{bg}\delta(t)=-T_g \qquad (22)$$

Equations (22) and (23) can be reduced to a single equation for a translational definite system using the DTE definition. A time-varying viscous damping could also be included by assuming equivalent viscous damping ratio ζ_e

$$m_e\ddot{\delta}(t)+C_e(t)\left[\dot{\delta}(t)-\dot{\varepsilon}(t)\right]+K_e(t)\left[\delta(t)-\varepsilon(t)\right]=F_e$$

$$m_e=\frac{J_{pz}J_{gz}}{r_{bg}^2J_{pz}+r_{bp}^2J_{gz}},\quad F_e=\frac{r_{bp}T_pJ_{gz}-r_{bg}T_gJ_{pz}}{r_{bg}^2J_{pz}+r_{bp}^2J_{gz}}$$

$$K_e(t)=\sum_{i=0}^{2}K_{e,i}(t)=\sum_{i=0}^{2}\frac{r_{bp}^2J_{gz}K_{p,i}(t)+r_{bg}^2J_{pz}K_{g,i}(t)}{r_{bg}^2J_{pz}+r_{bp}^2J_{gz}}$$

$$C_{e,i}(t)=2\zeta_e\sqrt{m_eK_e(t)}\approx 2\zeta_e\sqrt{m_e\bar{K}_e} \qquad (24a\text{-}e)$$

Here, m_e is the effective mass defined in the torsional-transverse direction and F_e is the effective external force due to the nominal torques applied at the pinion and gear. The periodical effective stiffness function $K_{e,i}(t)$ of i^{th} meshing mesh pair is piece-wise linear, and it incorporates contributions from both the mesh tooth stiffness and the sliding friction. The frictional influence on $K_{e,i}(t)$ is illustrated in Fig. 4, where a generic effective stiffness function is obtained by following a single tooth pair for three complete mesh cycles since ceil(σ) = 3.

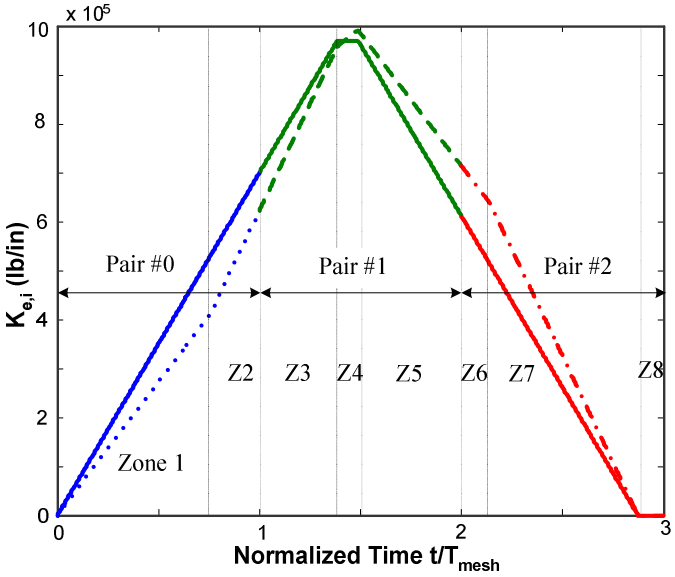

Figure 4: Individual effective stiffness $K_{e,i}(t)$ along contact zone. Key: —— tooth pair #0 (μ = 0), —— tooth pair #1 (μ = 0), —— tooth pair #2 (μ = 0); ..... tooth pair #0 (μ = 0.4), - - - tooth pair #1 (μ = 0.4), - · - tooth pair #2 (μ = 0.4).

The effect of sliding friction is illustrated over eight contact zones of Fig. 4: When μ = 0 (no friction), $K_{e,i}(t)$ has a symmetric trapezoidal profile, when high sliding friction is introduced with μ = 0.4, additional discontinuities in the slope emerge during the transitions from Zone 1 to Zone 2, as well as from Zone 6 to Zone 7. These correspond to the conditions when the contact line reaches or leaves the pitch line. Note that the stiffness functions are piece-wisely continuous due to the gradual approaching and recess motions of the helical gear pair. Compared with the square-wave shaped tooth stiffness function of a spur gear pair [1-3], this should be more favorable as lower vibro-acoustic response levels would be expected.

For multiple tooth pairs in contact, the effective stiffness $K_e(t)$ of Eq. (24) should include contributions from all meshing tooth pairs. Define index j for the j^{th} interval (with a constant slope) and define the generic periodic stiffness function $K_{e,j}(t)$ over m piece-wise intervals within one mesh cycle:

$$K_{e,j}(t)=K_{e,j}(t+T)=K_{e,j-1}+\frac{K_{e,j}-K_{e,j-1}}{t_j-t_{j-1}}\cdot\left(t-t_{j-1}\right) \qquad (25)$$

For the example case with individual $K_{e,i}(t)$ (i = 0, …, 2) of Fig. 4, the combined $K_{e,j}(t)$ (j = 1, …, 6) are calculated over six contact regions within one mesh cycle. Since the slope is constant within each region, only the stiffness values $K_{e,j}$ at the starting and ending time instants are needed with $K_{e,6} = K_{e,0}$ due to periodicity. The time instants t_i of each region within one period could be determined based on Fig. 2(b) as follows: $t_0 = 0$; $t_1 = (L_{EH}/\lambda)T$; $t_2 = (L_{CQ}/\lambda)T$; $t_3 = (L_{CD}/\lambda)T$; $t_4 = (L_{AP}/\lambda)T$; $t_5 = (L_{EG}/\lambda)T$; $t_6 = T$. Table 1 lists the relationship between the six contact regions defined for the combined stiffness function $K_{e,j}(t)$ and the eight contact zones defined for individual meshing tooth pair $K_{e,i}(t)$. Although the number of contact zones/regions depends on gear geometry, proposed modeling strategy could be implemented to other helical gear pairs.

Table 1 Relationship between contact zones and contact regions for the NASA-ART helical gear pair

Contact Region	Contact Zones of Fig. 2(b)		
	Pair #0	Pair #1	Pair #2
1	Z1	Z3	Z6
2	Z1	Z3	Z7
3	Z1	Z4	Z7
4	Z1	Z5	Z7
5	Z2	Z5	Z7
6	Z2	Z5	Z8

Figure 5 compares the combined $K_{e,j}(t)$ and the individual $K_{e,i}(t)$ over one period. Observe that the profile of $K_{e,j}(t)$ resembles those of individual $K_{e,i}(t)$: Under 0 friction, $K_{e,j}(t)$ follows a symmetric trapezoidal pattern, where 4 piece-wise intervals exist within one mesh cycle. When the sliding friction is included, two additional discontinuities in the slope are introduced at the transitions from Region 1 to Region 2, as well as from Region 4 to Region 5. Hence, six piece-wise regions need to be analyzed for one complete mesh cycle. However, a high mean component exists for the combined $K_{e,j}(t)$, whose values are always positive (non-zero).

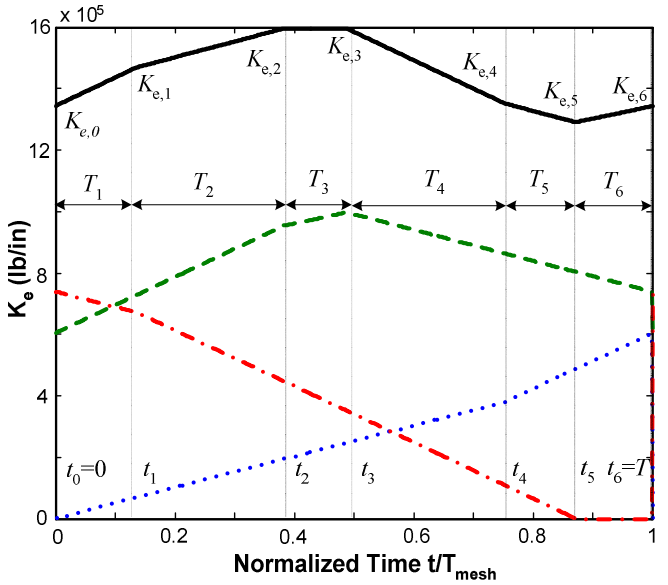

Figure 5: Piece-wise effective stiffness function defined in six regions within one mesh cycle with μ = 0.4. Key: .... tooth pair #0, - - - tooth pair #1, - · - tooth pair #2, –– combined stiffness function.

5 ANALYTICAL SOLUTIONS BY FLOQUET THEORY

Manish and Singh [2] suggested analytical solutions to the SDOF spur gear system model with periodic square-wave stiffness. For a helical gear pair, $K_{e,i}(t)$ varies periodically in a trapezoidal pattern; hence, the spur gear could be regarded as a special (limiting) case of the helical gear model where the slope of stiffness within each interval is zero rather than an arbitrary constant. We adopt a similar approach [2] to derive the closed-form analytical solutions of SDOF helical gear model.

Assume $\varepsilon(t)$ = 0 (perfect involute profile) and $C_e(t)$ = 0 (undamped oscillator), the parametrically excited system under a mean load F_e of Eq. (24) is simplified as follows:

$$m_e\ddot{\delta}(t)+K_e(t)\delta(t)=F_e \tag{26}$$

Floquet theory [12] is then applied to find analytical solutions for both free and force vibration responses. For the example helical gear pair, six contact regions need to be formulated with the influence of sliding friction. Hence, the equation of motion is represented in the state space form as follows:

$$\dot{X}(t)=G(t)X(t)+F(t),\ G(t+T)=G(t)$$

$$G(t)=\begin{cases} G_1(t) & 0\le t<t_1 \\ G_j(t) & t_{j-1}\le t<t_j\ (i=2...5) \\ G_6(t) & t_5\le t<T \end{cases}$$

$$X(t)=\begin{Bmatrix}\delta(t)\\ \dot{\delta}(t)\end{Bmatrix},\quad F(t)=\begin{Bmatrix}0\\ F_e/m_e\end{Bmatrix} \tag{27a-e}$$

The solution over one complete mesh cycle T is written in the form of a state transition matrix (Φ), as suggested by Richards [12]. For a piecewise periodic system, this matrix may further be decomposed into Φ_j over each contact regions [12], where the functions are continuously differentiable and analytical solutions to the homogeneous equation exist. The discrete transition matrix is given as:

$$\Phi(T,0)=\Phi(T,t_5)\cdots\Phi(t_2,t_1)\Phi(t_1,0) \tag{28}$$

Each $\Phi(t_j, t_{j-1})$ is evaluated from the Wronskian matrix (Π) as:

$$\Phi(t_j,t_{j-1})=\Pi(t_j)\Pi^{-1}(t_{j-1}),\ \ t_{j-1}\le t\le t_j \tag{29a}$$

$$\Pi(t)=\begin{bmatrix}\gamma_1 & \gamma_2\\ \dot{\gamma}_1 & \dot{\gamma}_2\end{bmatrix} \tag{29b}$$

Here, γ_1 and γ_2 are two basis solutions to the homogeneous equation $\dot{X}(t)=G(t)X(t)$. Use the periodic property of the state transition matrix, Floquet theory extends the calculated solutions to the subsequent states of the system that are apart by n mesh cycles. Thus, the state transition matrix over n cycles is given by:

$$\Phi(nT,0)=\Phi(T,0)^n \tag{30}$$

The dynamic responses are given as:

$$X(t)=\Phi(t,0)X(0)+\int_0^t\Phi(t,\tau)F(\tau)d\tau \tag{31a}$$

$$X(t+nT)=\Phi^n(T,0)X(t) \tag{31b}$$

Equations (28-31) are of significant importance. First, it drastically reduces the computational effort since the results calculated for one mesh cycle can be easily extended to other periods using matrix multiplication, which is computationally effective. Second, it allows an easier inversion of the matrix.

5.1 Free Vibration Response (to Initial Conditions)

Within the time interval $t_{j-1} \le t < t_j$, Eq. (26) is rewritten in the homogeneous form as follows:

$$\ddot{\delta}(t)+\left[a_j-2q_j\left(-\frac{2t}{t_j-t_{j-1}}+1\right)\right]\delta(t)=0\ \ t_{j-1}\le t\le t_j(j=1...6)$$

$$\beta_j=\frac{1}{m_e}\left(\frac{K_j-K_{j-1}}{t_j-t_{j-1}}\right),\quad \alpha_j=\frac{K_{j-1}}{m_e}-\beta_j t_{j-1}$$

$$a_j=\alpha_j+\frac{\beta_j(t_j-t_{j-1})}{2},\quad q_j=\frac{\beta_j(t_j-t_{j-1})}{4} \tag{32a-e}$$

With a change of variable $z_j=\alpha_j+\beta_j t$, Eq. (32) is converted into the Stoke's equation [12]:

$$\frac{d^2\delta}{dz_j^2}+\frac{z_j}{\beta_j^2}\delta=0 \tag{33}$$

A set of basis solutions are known over $t_{j-1} \le t < t_j$:

$$\gamma_1(t)=\sqrt{z_j}J_{1/3}(\sigma_j),\ \ \gamma_2(t)=\sqrt{z_j}J_{-1/3}(\sigma_j) \tag{34a-b}$$

where $J_{\pm1/3}(\sigma_j)$ is the Bessel function of the first kind of order ±1/3 and $\sigma_j=2z_j^{3/2}(3\beta_j)^{-1}$. Utilize the recurrence relation of Bessel functions to find the Wronskian matrix as:

$$\Pi_j(t)=\begin{bmatrix}\sqrt{z_j}\,J_{1/3}(\sigma_j) & \sqrt{z_j}\,J_{-1/3}(\sigma_j)\\ z_j\,J_{-2/3}(\sigma_j) & -z_j\,J_{2/3}(\sigma_j)\end{bmatrix} \quad (35a)$$

$$\Pi_j^{-1}(t)=-\frac{2\pi}{3\sqrt{3}\beta_j}\begin{bmatrix}-z_j\,J_{2/3}(\sigma_j) & -\sqrt{z_j}\,J_{-1/3}(\sigma_j)\\ -z_j\,J_{-2/3}(\sigma_j) & \sqrt{z_j}\,J_{1/3}(\sigma_j)\end{bmatrix} \quad (35b)$$

Note than Eq. (34-35) are valid only for those conditions when $z_j > 0$. Conversely, when z_j is negative (or zero), the Wronskian matrices are derived in terms of the modified Bessel functions of the first kind (or Gamma functions) which could be treated in a similar matter. However, for the SDOF helical gear model with a high (and positive) mean component, all z_j have positive values so that Eqs. (34-35) hold. Also, for the intervals with a negative slope β_j (such as for contact regions 4 and 5 of Fig. 5), the corresponding σ_j also takes negative values, which lead to complex $\Pi_j(t)$ generated by the Bessel functions in Eqs. (34-35). Nevertheless, due to the supplemental phase relationship between $\Pi(t_j)$ and $\Pi^{-1}(t_{j-1})$, the state transition matrix $\Phi(t_{j-1}, t_j) = \Pi(t_j)\Pi^{-1}(t_{j-1})$ still takes real values within each interval $t_{j-1} \le t < t_j$. Thus, responses to initial conditions $X(0)=\{\delta(0),\dot{\delta}(0)\}^T$ are as derived as follows:

$$X(t)=\Phi(t-nT,0)\Phi(T,0)^n\,X(0),\left(0\le t-nT<T\right) \quad (36)$$

where $\Phi(T, 0)$ is the discrete transition matrix. Here. $\Phi(t–nT, 0)$ needs to be evaluated similar to Eq. (28) over the last cycle.

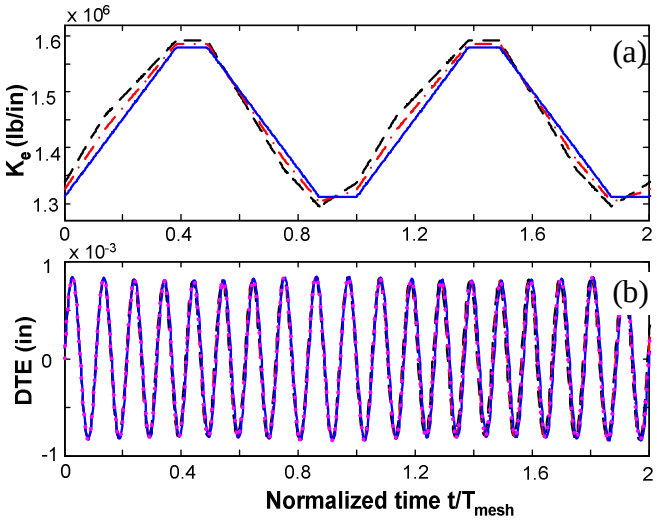

Figure 6: (a) Effective stiffness and (b) homogeneous periodic responses predictions within two mesh cycles given x_0 = 2e-6 in, v_0 = 20 in/s at Ω_p = 1000 RPM. Key: **––**, μ = 0 (Analytical solution by the Floquet theory); **- - -**, μ = 0.2 (Analytical); **.....**, μ = 0.2 (Numerical); **- - - ,** μ = 0.4 (Analytical).

Figure 6 compares the homogeneous responses given initial condition x_0 = 2e-6 in, v_0 = 20 in/s at Ω_p = 1000 RPM, as predicted by the analytical (Floquet theory) and the numerical (SIMULINK by using an ODE45 numerical integration algorithm) solutions. Since the numerical solution completely overlaps with the analytical (Floquet theory) prediction, only one set of comparison results are given at μ = 0.2. Observe that increasing sliding friction changes the slopes of the effective stiffness function $K_{e,j}(t)$, while such effect does not seem to be significant in the DTE response. This is because that the undamped responses are dictated by the dynamic components at the system natural frequency $f_n = \sqrt{\bar{K}_e}/\left(2\pi\sqrt{m_e}\right)$, where $\bar{K}_e$ is the averaged stiffness. For the example case of Fig. 6, f_n is found to be close to $9.5f_{mesh}$, where f_{mesh} is the first mesh frequency at Ω_p = 1000 RPM. Low side bands around $8.5f_{mesh}$ and $10.5\ f_{mesh}$ may also be present due to the frequency modulation effects.

5.2 Forced Response

For the LTV system of Eq. (26), the state transition matrix can be applied to compute the forced vibration response given a periodic excitation. The tractability of the solution depends both on the excitation characteristics and the nature of the state transition matrix. In general, this problem is solved by expanding the forcing function as well as the time-varying parameters in terms of Fourier coefficients. Clearly, this will lead to errors due to truncation of modes and also significantly increase the computations [2]. For our example gear pair, three (or six) piecewise linear segments need to be considered for each mesh cycle without (or with) the influence sliding friction. All integrals associated with the Floquet theory could be analytically found given a mean torque excitation. However, as the number of piecewise linear segments increases within a mesh cycle, such as for the realistic stiffness profile, analytical solutions could become more tedious, and thus some computational effort would then be required.

The forced response of the system is formulated as follows:

$$X(t)=\Pi(t)\Pi^{-1}(t)X(0)+\int_0^t\Pi(t)\Pi^{-1}(\tau)F(\tau)d\tau \quad (37)$$

Given the initial condition response $\Pi(t)\Pi^{-1}(t)X(0)$ already derived in Eq. (36), only the particular response term must be derived by applying $\Phi(t,0)=\Phi(t,\tau)\Phi(\tau,0)$ for any τ:

$$\begin{aligned}X(t)&=\Phi(t,0)\left[\int_0^{nT}\Phi^{-1}(\tau,0)F(\tau)d\tau+\int_{nT}^{t}\Phi^{-1}(\tau,0)F(\tau)d\tau\right]\\&=\Phi(t,0)\left[H_1(n)+H_2(t)\right]\end{aligned} \quad (38)$$

The solution is found in two parts, namely for integral number of mesh cycles (H_1) and that for the last cycle (H_2) [2]. The expression for $H_1(t)$ for n complete cycles is found as follows:

$$H_1(n)=\sum_{i=1}^{n}\int_{(i-1)T}^{iT}\Phi_i^{-1}(\tau,0)F(\tau)d\tau \quad (39)$$

Apply the Floquet theory and define $\tau_0 = \tau + (i-1)T$ so that:

$$H_1(n)=\sum_{j=1}^{n}\left\{\begin{bmatrix}\left[\Phi^{-1}(T,0)\right]^{j-1}\cdot\\ \Pi_1(t_0)\int_0^{t_1}\Pi_1^{-1}(\tau)F(\tau_0)\,d\tau+\\ \Pi_1(t_0)\Pi_1^{-1}(t_1)\Pi_2(t_1)\int_{t_1}^{t_2}\Pi_2^{-1}(\tau)F(\tau_0)d\tau+\\ \Pi_1(t_0)\Pi_1^{-1}(t_1)\Pi_2(t_1)\Pi_2^{-1}(t_2)\Pi_3(t_2)\int_{t_2}^{t_3}\Pi_3^{-1}(\tau)F(\tau_0)\,d\tau+\ldots\end{bmatrix}\right\} \quad (40)$$

For the last cycle, the value of $H_2(t)$ depends on the positioning of time instant t in the whole mesh cycle. Hence, solutions are derived within each of the piecewise linear segment as follows in Eq. (41),

$$H_2(t)=\left[\Phi^{-1}(T,0)\right]^n\left[\Pi_1(0)\int_0^{t-nT}\Pi_1^{-1}(\tau)F(\tau_0)\,d\tau\right]$$
$$=\left[\Phi^{-1}(T,0)\right]^n\times$$
$$\begin{cases}\Pi_1(0)\int_{t_1}^{t-nT}\Pi_1^{-1}(\tau)F(\tau_0)d\tau; \\ (t_0\le t-nT<t_1) \\ \left[\begin{array}{l}\Pi_1(0)\int_0^{t_1}\Pi_1^{-1}(\tau)F(\tau_0)\,d\tau+\\ \Pi_1(0)\Pi_1^{-1}(t_1)\Pi_2(t_1)\int_{t_1}^{t-nT}\Pi_2^{-1}(\tau)F(\tau_0)d\tau\end{array}\right]; \\ (t_1\le t-nT<t_2) \\ \cdots\cdots \\ \left[\begin{array}{l}\Pi_1(0)\int_0^{T}\Pi_1^{-1}(\tau)F(\tau_0)\,d\tau+\ldots\\ +\Pi_1(0)\Pi_1^{-1}(t_1)\Pi_2(t_1)\Pi_2^{-1}\cdots\Pi_j(t_{j-1})\int_{t_{j-1}}^{t-nT}\Pi_j^{-1}(\tau)F(\tau_0)\,d\tau\end{array}\right]; \\ (t_{j-1}\le t-nT<t_j,\ t_6=T)\end{cases} \tag{41}$$

where $\tau_0 = \tau + nT$, and all matrices have been analytically derived except for the $\int_0^0\Pi^{-1}(\tau)F(\tau)\,d\tau$ integral, which could be analytically found by using Eq. (42), where the *LommelS1* are the Lommel function. Note that the mean term in the forcing function $F(t) = \{0 \;\; F_e/m_e\}^T$ could be taken out of the integral;

$$\int zJ_{2/3}(\sigma)dt=-\sqrt{z}J_{-1/3}(\sigma),\quad \int zJ_{-2/3}(\sigma)dt=\sqrt{z}J_{1/3}(\sigma)$$
$$\int-\sqrt{z}\,J_{-1/3}(\sigma)\,dt=\frac{4\sigma}{3}J_{-1/3}(\sigma)L_1+\sigma J_{-4/3}(\sigma)L_2$$
$$\int\sqrt{z}\,J_{2/3}(\sigma)\,dt=-\frac{2\sigma}{3}J_{1/3}(\sigma)L_3-\sigma J_{-2/3}(\sigma)L_4$$
$$L_1=LommelS1(-1,-\frac{4}{3},\frac{2}{3}\beta z^{\frac{3}{2}}),\quad L_2=LommelS1(0,-\frac{1}{3},\frac{2}{3}\beta z^{\frac{3}{2}})$$
$$L_3=LommelS1(-1,-\frac{2}{3},\frac{2}{3}\beta z^{\frac{3}{2}}),\quad L_4=LommelS1(0,\frac{1}{3},\frac{2}{3}\beta z^{\frac{3}{2}}) \tag{42a-h}$$

In Fig. 7, analytical solutions of forced response as given by Eqs. (37-42) compare well with numerical integration results (obtained from SIMULINK), given operational conditions $C_e(t) = 0$, x_0 = 2e-6 in, v_0 = 20 in/s, T_p = 2000 lb-in, μ = 0.2 and Ω_p = 1000 RPM. Here, the $K_e(t)$ profile is the same as Fig. 6(a) with μ = 0.2, thus six piece-wise contact regions need to be considered within each mesh cycle. Similar to the undamped homogeneous response, the forced responses are also dominated by the dynamic component at the system natural frequency as well as side bands due to the frequency modulation effects. Such resonances, however, are efficiently controlled by viscous damping, while the spectra at the forced mesh harmonics are insensitive to the viscous damping. Consequently, if any mesh harmonic is away from the resonant frequency, one can obtain the dynamic responses (which should share the same features as damped responses) by filtering out the resonant components in the frequency domain. For our example case, a low pass filter is used since $f_n >> f_{mesh}$.

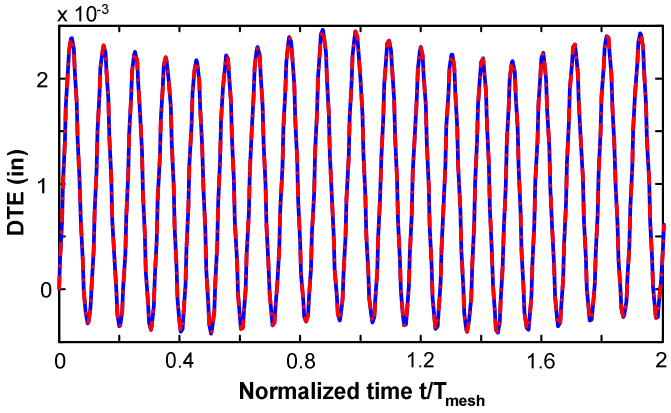

Figure 7: Predictions of (undamped) forced periodic responses within two mesh cycles given x_0 = 2e-6 in, v_0 = 20 in/s, T_p = 2000 lb-in, μ = 0.2 and Ω_p = 1000 RPM. Key: **––**, Analytical (Floquet theory); **- · -**, Numerical.

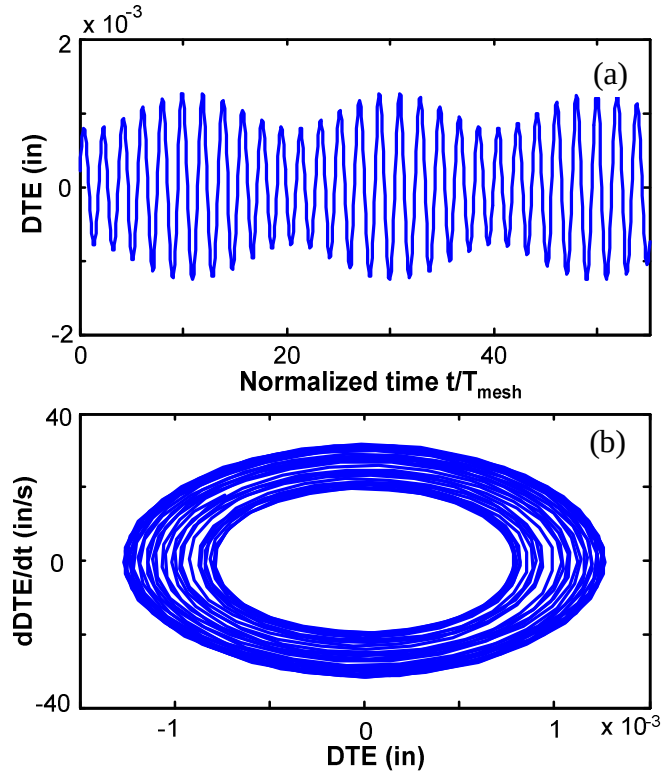

Figure 8: Long-term stability of free vibration (homogeneous) response given x_0 = 2e-6 in, v_0 = 20 in/s, μ = 0.2 and Ω_p = 18,000 RPM: (a) Time domain response; (b) Phase plane plot.

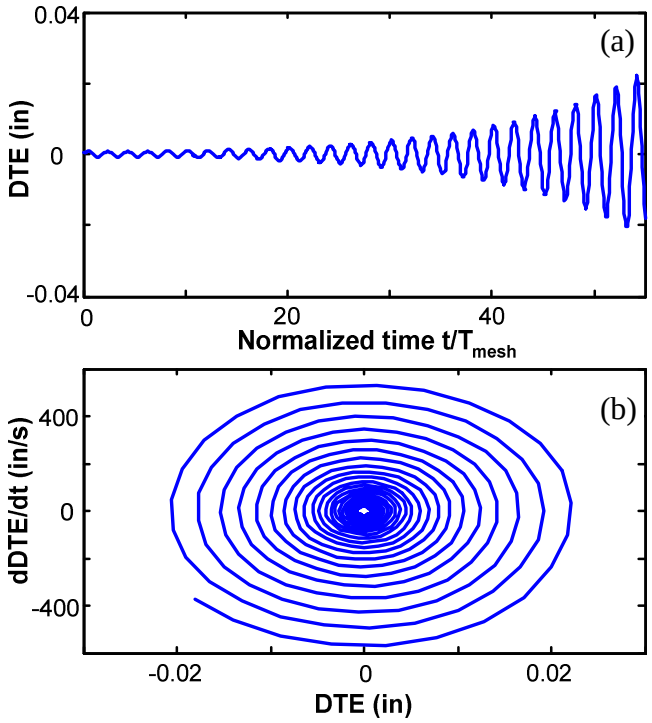

Figure 9: Unstable free vibration (homogeneous) response given x_0 = 2e-6 in, v_0 = 20 in/s, μ = 0.2 and Ω_p = 19,000 RPM: (a) Time domain response; (b) Phase plane plot.

6 CONCLUSION

Analytical models of a helical gear pair have been developed to examine the effect of sliding friction on the dynamic transmission error. Linear time-varying formulations (with parametric excitations) have been developed for both 6DOF and SDOF models. The effect of sliding friction is quantified by an effective mesh stiffness term. Floquet theory has been successfully used to obtain closed-form solutions given periodic piece-wise linear tooth stiffness function. Analytial responses to both initial conditions and forcing function under a nominal preload are derived and validated by comparing with numerical simulations. Finally, stability studies are briefly conducted when the gear pair operates close to unstable regions. For instance, when Ω_p = 18,000 RPM such that $f_{mesh}(t)/f_n$ is close to 2, long term stability is observed in time domain response as well as in the phase plot, as illustrated in Fig. 8. On the other hand, when Ω_p = 19,000 RPM such that $f_{mesh}(t)/f_n$ falls within the unstable region, the amplitude of the homogeneous response continues to grow, as shown in Fig. 9. Although the coefficient of friction μ is assumed to be high for the example case for demonstrative purpose, the same algorithm could be implemented for realistic conditions where smaller values of μ are expected. Future work will focus on such stability and other analytical response issues [14].

7 ACKNOWLEDGMENTS

We gratefully acknowledge support from the U.S. Army Research Office (grant number DAAD19-02-1-0334 [15]). Prof. G. Pavic (INSA Lyon, France) is thanked for his support for the first author during the preparation of this paper. Finally, we acknowledge Dr. T. Rook (Goodrich Co.) for his comments and suggestions.

8 REFERENCES

[1] Vaishya, M. and Singh, R., 2003, "Strategies for Modeling Friction in Gear Dynamics," *ASME J. Mech. Des.*, **125**, pp. 383-393.

[2] Vaishya, M. and Singh, R., 2001, "Analysis of Periodically Varying Gear Mesh Systems with Coulomb Friction using Floquet Theory," *J. Sound Vib.*, **243**(3), pp. 525-545.

[3] Vaishya, M. and Singh, R., 2001, "Sliding Friction-Induced Non-Linearity and Parametric Effects in Gear Dynamics," *J. Sound Vib.*, **248**(4), pp. 671-694.

[4] Velex P. and Cahouet V., 2000, "Experimental and Numerical Investigations on the Influence of Tooth Friction in Spur and Helical Gear Dynamics," *ASME J. Mech. Des.*, **122** (4), pp. 515-522.

[5] Velex, P. and Sainsot, P., 2002, "An Analytical Study of Tooth Friction Excitations in Spur and Helical Gears," *Mech. Mach. Theory*, **37**, pp. 641-658.

[6] Lundvall, O., Strömberg, N. and Klarbring, A., 2004, "A Flexible Multi-Body Approach for Frictional Contact in Spur Gears," *J. Sound Vib.*, **278**(3), pp. 479-499.

[7] He, S., Gunda, R. and Singh, R., 2007, "Effect of Sliding Friction on the Dynamics of Spur Gear Pair with Realistic Time-Varying Stiffness," *J. Sound Vib.*, **301**, pp. 927-949.

[8] He, S., Gunda, R., and Singh, R., 2007, "Inclusion of Sliding Friction in Contact Dynamics Model for Helical Gears," *ASME J. Mech. Des.*, **129**, pp. 48-57.

[9] Borner, J. and Houser, D. R., 1996, "Friction and Bending Moments as Gear Noise Excitations," *SAE Trans.*, 105(6), pp. 1669-1676.

[10] Padmanabhan, C., Barlow, R. C., Rook, T. E. and Singh, R., 1995, "Computational Issues Associated with Gear Rattle Analysis," *ASME J. Mech. Des.*, **117**, pp. 185-192.

[11] Helical3D (CALYX software), 2003, "Helical3D User's Manual," ANSOL Inc., Hilliard, OH.

[12] Richards, J. A., 1983, *Analysis of Periodically time-varying Systems*, New York, Springer.

[13] Den Hartog, J. P., 1956, *Mechanical Vibrations*, New York, Dover Publications.

[14] He, S., and Singh, R., 2007, "Dynamic Transmission Error Prediction of Helical Gear Pair under Sliding Friction using Floquet Theory," submitted to *ASME J. Mech. Des.*

[15] Singh, R., 2005, "Dynamic Analysis of Sliding Friction in Rotorcraft Geared Systems," technical report submitted to the Army Research Office, grant number DAAD19-02-1-0334.